THREE-DIMENSIONAL BEAMFORMING FOR WIND TUNNEL APPLICATIONS USING ESM BASED TRANSFER FUNCTIONS

Joannès Chambon, Thibaut Le Magueresse, Olivier Minck, Jérôme Antoni

BeBeC-2020-S9

THREE-DIMENSIONAL BEAMFORMING FOR WIND TUNNEL APPLICATIONS USING ESM BASED TRANSFER FUNCTIONS

Joannès Chambon[1,2], Thibaut Le Magueresse[1], Olivier Minck[1] and Jérôme Antoni[2]
[1]MicrodB
28 chemin du Petit Bois, 69130, Écully, France
[2]Laboratoire Acoustique et Vibration
25 Avenue Jean Capelle, 69100, Villeurbane, France

Abstract

As an inverse problem, sound source localization in three dimensions relies on two distinct cornerstones. One is the physical model chosen to describe the acoustic propagation of the sources to identify and the other is the algorithmic process used to derive information from measured acoustic data. Mainly focusing on the first point, an Equivalent Source Method (ESM) aiming at the simulation of realistic Frequency Response Functions (FRF) is proposed in this paper. The underlying idea is to substitute the acoustic behaviour of a radiating object by a set of acoustic monopoles calibrated with respect to the boundary condition on its skin. Such a method allows to perform 3D Conventional Beamforming (CBF) with FRF taking into account the acoustic environment and the influence structure. Misleading sound source localization outcomes due to ground reflections or diffraction are therefore prevented.

As a first step, the ESM process is validated thanks to the Spherical Related Transfer Function which provides a rigorous analytical framework for FRF comparison. ESM boils down to an inverse problem in itself upstream to CBF, and various ways of solving it are assessed. With a view to present an industrial application, FRF are computed on a car mesh to carry out 3D CBF with the experimental pressure scattered by an omnidirectional source placed near the rear-view mirror, measured by a 160 microphones top array and two 100 microphones side arrays in the Daimler automotive wind tunnel.

Finally, a strategy to include the contribution of wind tunnel convective effects at low Mach number is investigated. To this end, a geometric routine based on Amiet's model is coupled with the ESM boundary condition step and assessed on wind tunnel measurements.

Introduction

With the increasingly widespread demand for three dimensional acoustic imaging, the use of well-known methods such as CBF that proved to be reliable for bidimensional source localization turns to raise a significant collection of issues. Battista [1] pointed out that a planar microphone arrays feature a poor spatial resolution in its normal direction and may struggle to deal with potential sources at such uneven distances from its center.

Besides, source localization on a three dimensional radiating object is likely to get tricky when the measured acoustic field under scrutiny is the combination of scattered and reflected waves [2].

In order to address these problems, combining several planar arrays covering the sources appears to be a natural solution. A Multiplicative Cross Spectral Beamforming [3], suitable with multiple array imaging, was proposed and tested for the detection of compact sources in an uniform flow.

Bearing in mind three dimensional imaging for wind tunnel applications, the approach of this paper is slightly different since the emphasis is put on the computation of enhanced acoustic transfer functions between the potential sources and the antenna. Already extensively used as an alternative to Boundary Element Methods for the simulation of acoustic radiated fields [4–6], the Equivalent Source Method is slightly derived from its original role to compute acoustic transfer functions thanks to the reciprocity principle [7–9]. Notably, ESM for FRF computation discussed in this paper should not be mistaken with the ESM as an imaging method in itself. In the latter case, ESM denotes the reconstruction of equivalent acoustic sources placed within the object [10] or on its skin [11–13] under a free field assumption. In contrast, the ESM under scrutiny in this paper refers to the algorithm used for the simulation of complex acoustic transfer functions upstream of the imaging process.

The first section is a brief statement of the acoustic inverse problem treated in this paper and its formalism. The linkage between the ESM and the computation of FRF suitable for 3D beamforming is then presented, including the validation of the overall process with respect to the Spherical Related Transfer Function (SRTF) [14]. In the third section, refinements are proposed to take into account the ground reflections and shear layer refraction effect commonly observed during wind tunnel measurements. The last section is dedicated to the practical results of the method on measurements made in Daimler wind tunnel, with a discussion about further potential improvements.

1 Acoustic inverse problem

Given pressure signals measured by a set of M microphones, the estimation of the associated monopolar sources on the skin of the radiating object described by a mesh of N nodes boils down to the following formulation :

$$\boxed{\textit{Find} \quad \mathbf{q} \in \mathbb{C}^N \quad \textit{that satisfies} \quad \mathbf{p} = \mathbf{H}\mathbf{q}.} \tag{1}$$

Where $\mathbf{H} \in \mathbb{C}^{M \times N}$ must account for the acoustic propagation model between the sources and the microphones.

In practical, the measured signals are assumed ergodic and Eq.1 is solved in the frequency domain. In that case, the CBF provides a direct quadratic formulation for the sources as :

$$\forall j \leq N, \qquad \left|q_j\right|^2 = \frac{\mathbf{H}_{\cdot,j}^{\mathrm{H}} \mathbf{S}_{pp} \mathbf{H}_{\cdot,j}}{\left\|\mathbf{H}_{\cdot,j}\right\|^4}, \tag{2}$$

where $\mathbf{H}_{\cdot,j}$ denotes the j^{th} column of $\mathbf{H}$, $\mathbf{H}_{\cdot,j}^{\mathrm{H}}$ its conjugate transpose and $\mathbf{S}_{pp}$ the Cross Spectral Matrix (CSM)

$$\mathbf{S}_{pp} = \mathbf{p}\mathbf{p}^{\mathrm{H}}. \tag{3}$$

Acoustic Transfer Functions

Given the context described above, the FRF can be formally defined for each frequency as

$$\forall i \leq M, j \leq N, \qquad \mathbf{H}_{i,j} = \frac{p_i^j}{q_j}, \tag{4}$$

where p_i^j refers to the pressure induced by a volumic flow q_j at the j^{th} node measured at the i^{th} microphone. It ideally translates every physical feature likely to affect the sound propagation : diffraction around the object, reflection on the ground, aeroacoustic contribution, etc.

The most common way to fill $\mathbf{H}$ is to assume a free field propagation, i.e. to consider that each nodes is a potential monopolar source detected by the microphone arrays. In that case, the wavenumber k, the density ρ and the distance between control points and microphones $\left(r_{ij}\right)_{i\leq M, j\leq N}$ allow to directly compute

$$\mathbf{H}_{i,j} = -\mathrm{i}\omega\rho \frac{e^{\mathrm{i}kr_{ij}}}{4\pi r_{ij}}. \tag{5}$$

The $+\mathrm{i}kr$ convention is assumed in the rest of the paper.

Such a model offers on the one hand the advantage of being numerically robust and convenient for real time sound source identification. On the other hand, any additional boundary condition introduced by the presence of a scattering object or a reflecting ground is totally ignored in first approach and misleading sources are likely to be highlighted.

2 Equivalent Source Method for FRF computation

2.1 Reciprocity

Regarding Eq.4, the problematic of FRF construction seemingly falls into the scope of the reciprocity principle established for various types of sources [9, 15] : instead of identifying the pressure at the antenna given acoustic sources on the object, the FRF may also be understood as the ratio between the volumic flow of a source placed on a

microphone position and the pressure taken on the skin of the object. In the present context, the transfer function $\mathbf{H}$ becomes

$$\mathbf{H} \in \mathbb{C}^{M \times N} \quad such\ as \quad \mathbf{H}_{i,j} = \frac{p_j^i}{q_i} \quad \forall i \leq M, j \leq N, \tag{6}$$

and its Hermitian adjoint $\mathbf{H}^\dagger$ brings back to the initial definition of Eq.4.

This new approach paves the way for numerical simulations methods allowing to compute the acoustic field of a monopole scattered by the object.

2.2 Equivalent Sources Method : concept and benefits

The ESM was originally designed to compete with Boundary Element Method (BEM) for the simulation of scattered acoustic waves [6, 16]. Its underlying principle may be resumed as followed : considering a scattering object, N_s artificial sources of volumic flows $(\tilde{q}_k)_{k \leq N_s}$ are firstly placed inside its boundary Γ. This set of sources is then configured to meet the boundary condition on Γ so that their combined contributions could be considered as *equivalent* to the real presence of the object.

The theoretical statement of this approach was given by Koopman [4] and relies on the well-posedness of the problem. If the Helmholtz problem with its boundary condition is well posed, the pressure field resulting from a linear combination of fundamental solutions and satisfying the boundary conditions (b.c.) necessarily matches with the unique solution oustide Γ.

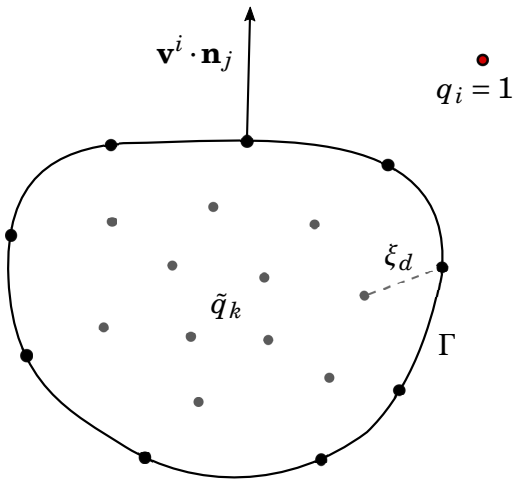

Fig. 1 - *ESM set up for FRF identification. Equivalent sources* $(\tilde{q}_k)_{k \leq N_s}$ *(in grey) are adjusted to counter balance the normal velocity induced by a unitary source* q_i *at every control points on* Γ.

For the sake of consistency with the industrial applications, an homogeneous Neumann boundary condition is considered in this paper on the discretized skin (i.e. perfectly rigid structure).

The calibration of equivalent sources placed inside the scattering object basically pertains to another intrinsic inverse problem. Their primary role is to offset the incident normal velocity to ensure the b.c. : if as on Fig-1 the incident field is the one of a unitary monopole located on the i^{th} microphone position, the compensating sources $\left(\tilde{q}_k^i\right)_{k\leq N_s}$ are mathematically established by

$$\boxed{\textit{Find} \quad \tilde{\mathbf{q}}^i \in \mathbb{C}^{N_s} \quad \textit{that satisfies} \quad \mathbf{v}^i\mathbf{n}^\top = -\nabla\mathbf{G}\tilde{\mathbf{q}}^i.} \tag{7}$$

$\mathbf{v}^i \in \mathbb{C}^{N\times 3}$ denotes here the velocity induced by q_i (unitary) at each control points and $\mathbf{n} \in \mathbb{C}^{N\times 3}$ the normals to Γ. Noting θ_{ij} as the angle between $\mathbf{r}_{ij}$ and the normal to Γ at the j^{th} control point,

$$\forall j \leq N, \quad \left(\mathbf{v}^i\mathbf{n}^\top\right)_j = \frac{e^{\mathrm{i}kr_{ij}}}{4\pi r_{ij}^2}(1-\mathrm{i}kr_{ij})\cos\theta_{ij}. \tag{8}$$

In the same way, $\nabla\mathbf{G} \in \mathbb{C}^{N\times N_s}$ emphasize the transfer between the equivalent sources volumic flows and the corresponding normal velocities on the skin :

$$\forall j \leq N, \quad \forall k \leq N_s, \quad \nabla\mathbf{G}_{j,k} = \frac{e^{\mathrm{i}kr_{jk}}}{4\pi r_{jk}^2}(1-\mathrm{i}kr_{jk})\cos\theta_{jk}. \tag{9}$$

Once Eq.7 is solved for all $i \leq M$, the last step is to repropagate the equivalent sources towards the control points to get the pressure on Γ

$$\forall i \leq M, \quad \mathbf{p}^i = \mathbf{G}\tilde{\mathbf{q}}^i, \tag{10}$$

using a the monopolar volumic to pressure transfer function :

$$\forall j \leq N, \quad \forall k \leq N_s, \quad \mathbf{G}_{j,k} = -\mathrm{i}\omega\rho\frac{e^{\mathrm{i}kr_{jk}}}{4\pi r_{jk}}. \tag{11}$$

For the specific case of radiating structures, the main advantages of ESM compared to methods presented may be summed up as follows :

- ESM is a *meshless* process, which makes the $\mathbf{G}$ and $\nabla\mathbf{G}$ assembling step much easier to implement and faster than the mass/rigidity matrices of FEM. The coding effort is also considerably reduced.
- Most papers in the literature advise to consider fewer equivalent sources than control points [6]. Eq.7 thus often turns out to be an overdetermined problem that can be solved efficiently.
- The bridge between the acoustic propagation its numerical model is explicitly contained in $\mathbf{G}$ and $\nabla\mathbf{G}$. Appropriate modifications of those matrices thus enable to take into account more complex environments using for example Amiet's model for shear layer refraction or image sources for ground reflections.

For all those assets, the stability of the method and its precision is the other side of the coins. As of now, the added value of ESM highly depends on a large collection of

parameters more or less linked one to another.

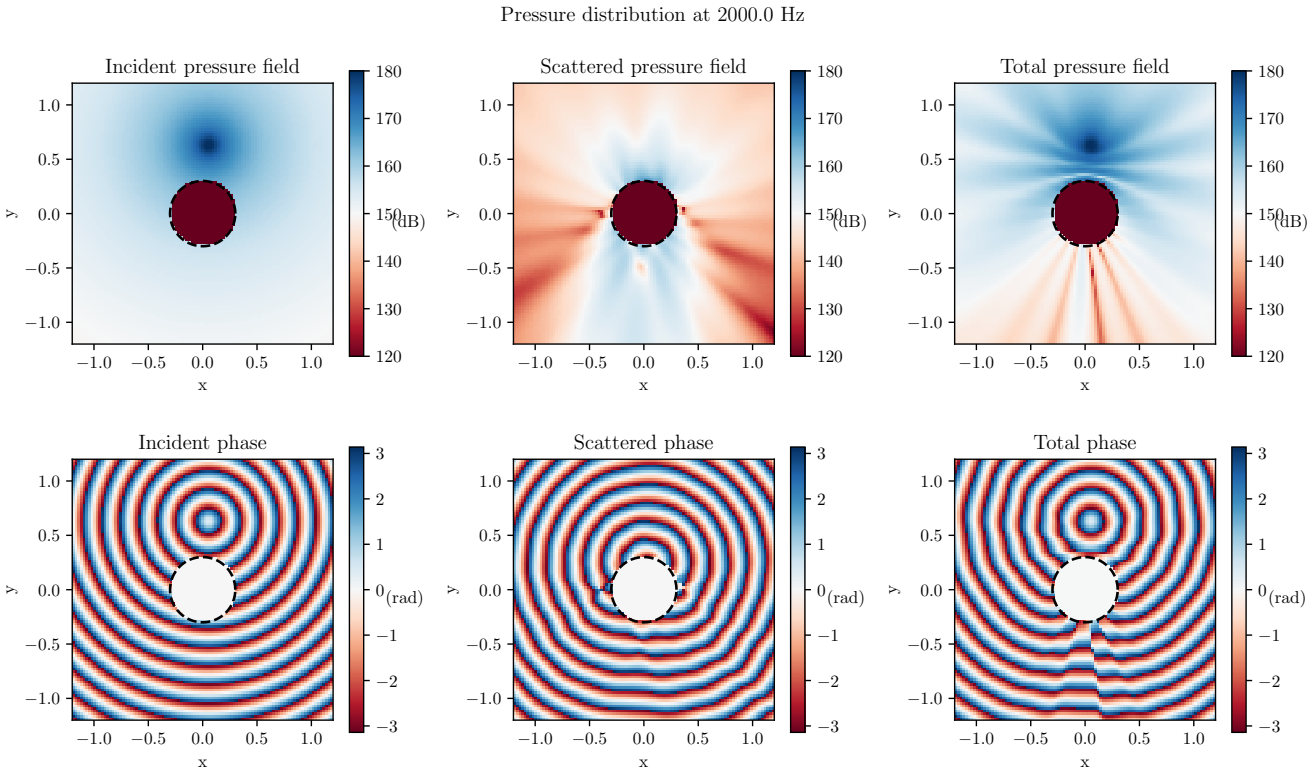

Fig. 2 - *Monopole scattered by a rigid sphere using 3D ESM (sectional view). The sphere is described by a 1000 sized point cloud. 500 equivalent sources randomly generated are tuned acoording to Eq.7 using a Moore Penrose pseudo-inverse, before being repropagated on a cross sectional regular grid for visualization.*

Number of equivalent sources

The optimal number of equivalent sources is an unresolved problem. A balance has to be found between too few sources unable to describe the complex scattered field of the object and a too high density of sources worsening the conditionning of the problem. Dunn and Tinetti stated for example that a ratio $\eta = N_s/M$ equal to 0.33 (i.e. three times less sources than control points) was optimal for their applications [16] while $\eta = 0.5$ turned out to provide better results for SRTF computation [17].

Position of equivalent sources

As the monopole formula presents a singularity at the origin, precautions must be taken to avoid unmanageable entries in $\nabla\mathbf{G}$. The minimum distance between sources and control points, called the *retreat distance* [18] noted as ξ_d on Fig-1, is a tricky question : if ξ_d is close to zero, propagation matrices are not numerically stable. If however ξ_d is chosen

too large, all the equivalent sources are very close from one another and $\nabla\mathbf{G}$ becomes ill-conditionned. Noteworthy is that no clear answers are given in the literature except on a case-by-case basis.

Another issue is the way of placing equivalent sources. A common solution is to consider a scaled replica of the object surface [16], but arranging them as a random cloud of points also yields encouraging results.

2.3 Validation

Well studied in the literature [14, 19], the Spherical Related Transfer Function (SRTF) stands for an analytical inclusion of diffraction for the specific case of a monopole scattered by a rigid sphere.

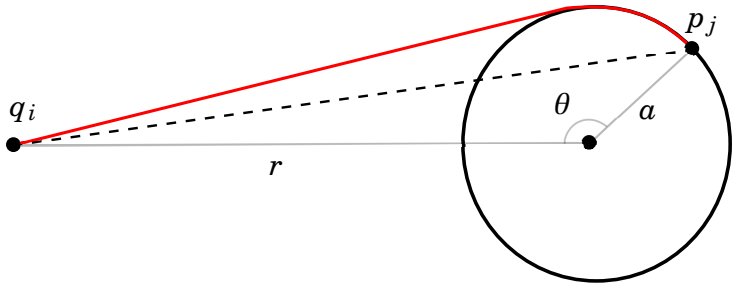

Fig. 3 - *Considering a rigid sphere of radius a, the SRTF analytically provides the pressure at p_j given a monopole of volumic flow q_i while taking into account the scattered path in red instead of the free field one (dashed).*

SRTF is used in this section as a validation case. Considering the setup of Fig-4, the transfer functions between two different control points and one microphone are computed using the ESM process as presented previously.

Transfer functions are computed up to 3 kHz so that the frequency limitation due to the number of control points on the sphere could be observed. Following Pereira's

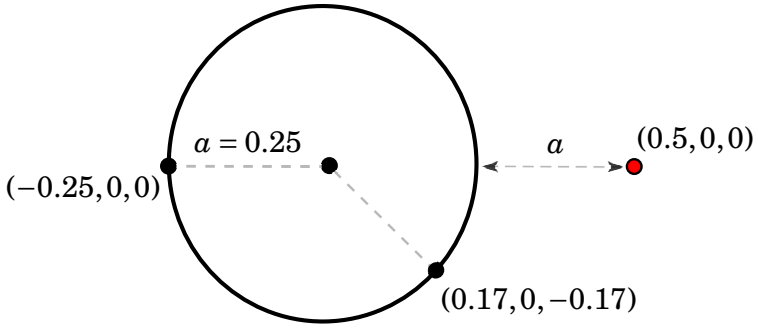

Fig. 4 - *Geometric values chosen for the SRTF validation. The first control point under scrutiny is located on the opposit to the microphone (in red) for the diffraction to be significant, while the second one it more similar to a free field propagation.*

recommandation [13] spherical harmonics are truncated at the 40^{th} order. For this first test $M = 1000$ control points a regularly placed on the sphere following a Fibonacci lattice, and $N_s = 500$ equivalent sources ($\eta = 0.5$) are used as advised by Asquier [17].

Comparing FRF for one control point/microphone couple is a basic but demanding exercise. The ESM process has to be relaunched for each frequency step since $\nabla\mathbf{G}$ is frequency dependant, which basically means that each point on Fig-5 is the result of one $M \times N_s$ system inversion.

A cross-validation with ACTRAN highlights the practical differences between FEM and ESM. Computing the acoustic scattering without any interpolation functions or element integrations eases the coding effort, as a relatively brief PYTHON ESM module matches with an industrial software for a basic propagation setup (see Fig-5).

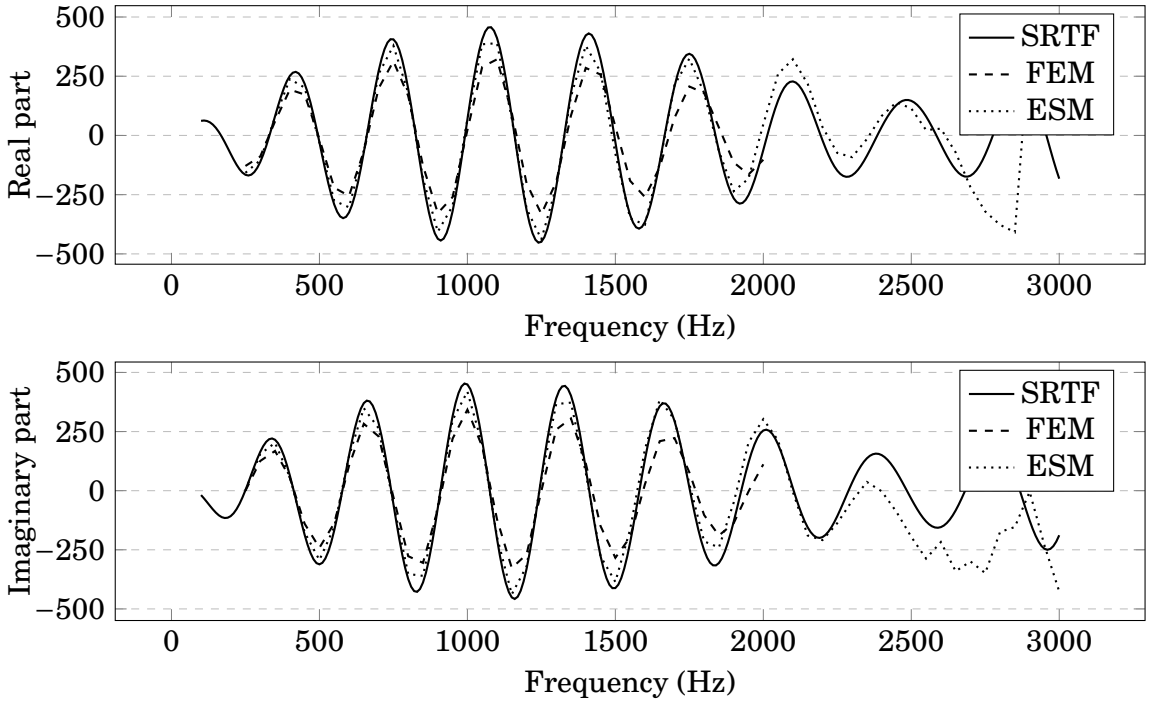

Fig. 5 - *Comparison of ESM with analytical SRTF and FEM results on the (-0.25,0,0) position. The 3D mesh used is composed of tetrahedrical elements of size $h =$ 0.022 (10 e.p.w. up to 1500 Hz), infinite elements of order 15 deal with the non reflection condition.*

Moreover, it should be noticed that the computation time for the highest frequency step reaches 15 seconds for the ESM [1] and approximately 90 seconds for FEM. The possibility of computing FRF at the end of the audible spectrum may be under consideration where the 10 elements per wavelength rule for FEM becomes unduly severe at such high frequencies.

[1] Sequential implementation, Intel Core i7 1.7GHz with 8 Go of RAM

3 Refined ESM for wind tunnel applications

3.1 Equivalent Image Sources

Considering the rigid ground of a wind tunnel, a first significative step is to include ground reflections in the FRF computation process. Facing the problem when applying an ESM to near field holography, Valdivia [20], proposed to complete Eq.7 with its copy assuming a symmetric set of equivalent sources underneath the ground. Formally, it leads to a new construction of the propagation matrices as

$$\forall j \leq N, \quad \forall k \leq N_s, \quad \mathbf{G}_{j,k} = -\mathrm{i}\omega\rho \left(\frac{e^{\mathrm{i}kr_{jk}}}{4\pi r_{jk}} + \frac{e^{\mathrm{i}kr'_{jk}}}{4\pi r'_{jk}} \right) \tag{12}$$

and

$$\forall j \leq N, \quad \forall k \leq N_s, \quad \nabla\mathbf{G}_{j,k} = \frac{e^{\mathrm{i}kr_{jk}}}{4\pi r_{jk}^2}(1-\mathrm{i}kr_{jk})\cos\theta_{jk} + \frac{e^{\mathrm{i}kr'_{jk}}}{4\pi r'^2_{jk}}(1-\mathrm{i}kr'_{jk})\cos\theta'_{jk}, \tag{13}$$

where r'_{jk}, θ'_{jk} respectively denote the distance and the angle between the symmetric of the equivalent source $\tilde{q}_k$ about the ground and the j^{th} control point. By construction, any control point located on the surface of the ground corresponds to the case

$$r_{jk} = r'_{jk}, \quad \theta_{jk} = \pi - \theta'_{jk} \tag{14}$$

and the velocity normal to the ground is ensured to be zero.

The advantage here is that the dimensions of the ESM inverse problem remains unchanged compared to the initial case with no ground reflections.

Validation with FEM results

Since the analytical SRTF does not take into account any ground reflection, validation is ensured by FEM. The 3D mesh already used in section 2.3 is used, by means of 10 elements per wavelength up to 2000 Hz. Sommerfeld is modeled with 30^{th} order infinite elements [21, 22], which is a large margin of error even if this parameter has to be set by trial and error. For each frequency, the validation is carried out through error maps on the scattered pressure field for both amplitude and phase,

$$\varepsilon_{\text{amp}} = 10\log\left(\left| \frac{p^{\text{ESM}}}{p^{\text{FEM}}} \right|^2 \right) \tag{15}$$

and

$$\varepsilon_{\text{phase}} = \left| \varphi^{\text{ESM}} - \varphi^{\text{FEM}} \right| \tag{16}$$

are computed on a regular grid including the sphere and the ground.

Paying attention to Fig-6, the results are almost similar from one numerical method to the other. Peaks of error are observed at the amplitude extrema, which indicates a minor approximation that may have appeared during the interpolation of the FEM result on

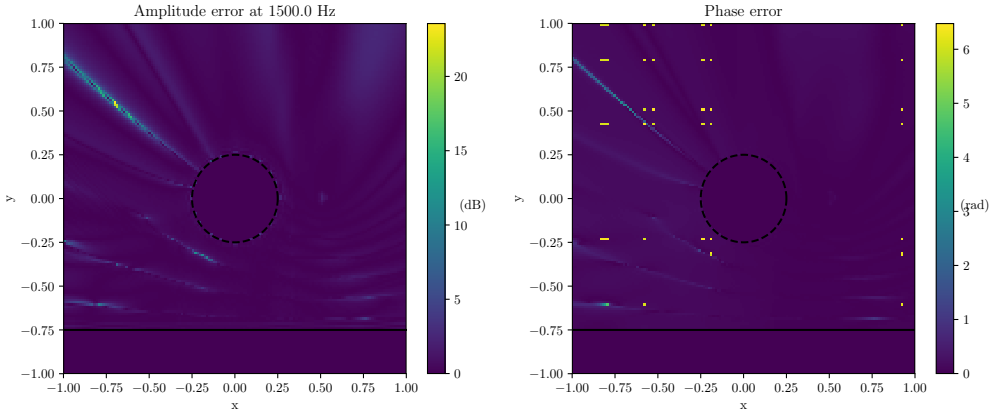

Fig. 6 - *Error of source image ESM scattered pressure against FEM simulation at 1500 Hz. Phase artifacts are due to the discontinuities between 0 and 2π*

the ESM grid. For the sake of generality, the same protocol was applied with different monopole position yielding the same accuracy in the reconstruction.

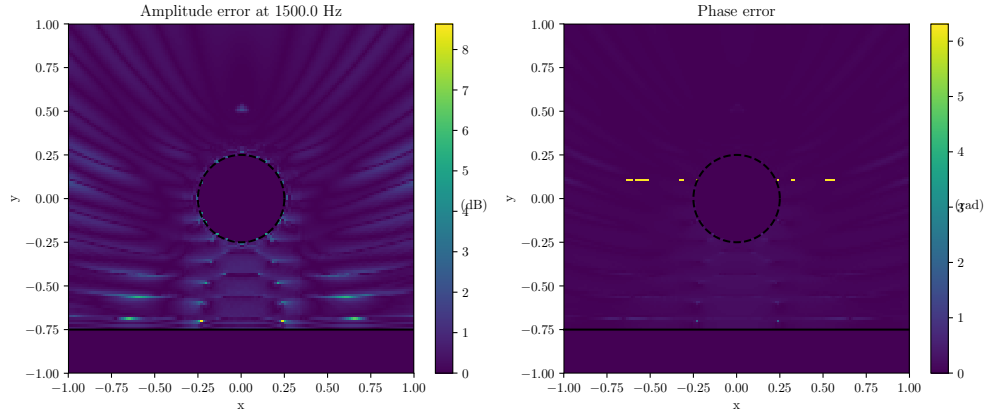

Fig. 7 - *Same as Fig-6 considering this time a monopole located at one radius above the sphere (0,0,0.5).*

3.2 Shear layer refraction

The last major gap between a free field propagation and a wind tunnel set up lies in the convective effect of the flow and the shear layer appearing at the nozzle boundary levels. Under the assumption of an uniform flow at low Mach number, Amiet [23] proposed an analogy with geometric optics to account for those phenomena.

Already widespread in 2D CBF softwares, a linkage with the ESM presented above is described in this section to compute FRF suitable with 3D wind tunnel source localization.

In the framework of section 2.2, Eq.8 is modified according to Amiet's model and the boundary condition part of the ESM inverse problems becomes :

$$\forall j \leq N, \quad \left(\mathbf{v}^i \mathbf{n}^\top\right)_j = \frac{e^{\mathrm{ik}\left(r_{ij}^{\mathrm{flow}} + r_{ij}^{\mathrm{ff}}\right)}}{4\pi\left(r_{ij}^{\mathrm{flow}} + r_{ij}^{\mathrm{ff}}\right)^2}\left(1 - \mathrm{ik}\left(r_{ij}^{\mathrm{flow}} + r_{ij}^{\mathrm{ff}}\right)\right)\cos\theta'_{ij}. \tag{17}$$

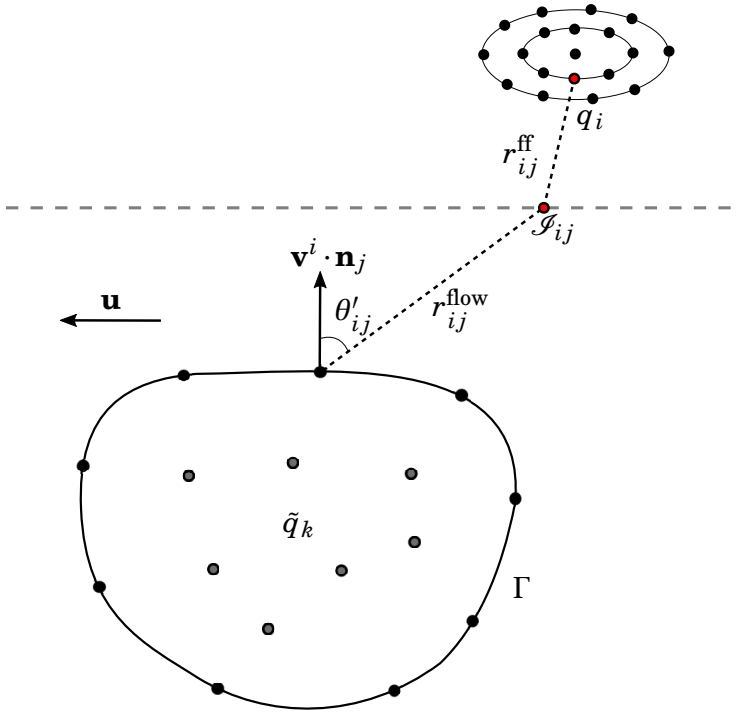

Fig. 8 - *Refracted acoustic path in the ESM set up. The acoustic transfer is now composed of the paths covered outside and within the flow r_{ij}^{ff} and r_{ij}^{flow}, the impact point $\mathscr{I}_{ij}$ on the shear layer being obtained thanks to a iterative integrating scheme [24].*

As described on Fig-8, the FRF computation is thus completed assuming new angles of incidence with impact points on the shear layer instead of the arrays reciprocal sources, and spatial $1/r$ attenuation resulting from the refracted paths.

The same treatment is applied to Eq.11 and the equivalent image sources as well in a straightforward, leading to FRF theoretically accounting for :

- Scattering effects modelled by to equivalent sources.
- Ground reflections because of the presence of equivalent image sources.
- Basic time shifts in the sources propagation caused by a shear layer assumed infinitely thin.

4 Imaging results on wind tunnel data

3D beamforming maps are discussed in this last section. The model under scrutiny is a car placed in DAIMLER wind tunnel meshed with 23 406 nodes. Two 100 microphones arrays located on both sides of the car and one 160 microphone array located above it were used for a 10 seconds measurement of the sound emitted by an omnidirectional source placed near the left rear-view mirror (see Fig-9) and scattered by the car. CSM were then computed featuring an $f_s = 51200$ Hz Fast Fourier Transform and a Hann window.

According to a short parametric study led on the Fig-5 case, the amount of equivalent sources was set to $\eta = 0.25$. The relatively small amount of equivalent sources may be considered suboptimal regarding the conclusions of section 2.2, but it turned out to be the maximum value suitable with the available calculation capacity.

In what follows, microphone positions and output actual levels in dB are not displayed for confidentiality reasons (the level dynamic range is absolute and was set to 12 dB on every plot).

Fig. 9 - *Omnidirectional source placed near the rear-view mirror.*

4.1 Beamforming without wind effects

ESM is assessed first with the wind tunnel unactivated. The aim is then to reconstruct the omnidirectional source next to rear view mirror without any aeroacoustic noise or sources in the first approach.

On Fig-10 are exposed as industrial reference the 2D CBF maps computed with MicrodB wind tunnel commercial software *AAT*, using free field transfer functions.

The full CSM of the whole 360 microphones array was then used to compute a 3D CBF with both free field and ESM FRF, for the results given in Fig-11.

As it stands, refined transfer functions seems to provide a more accurate localization of the source and avoids the residual sources on the windshield very likely caused by the poor resolution of side arrays in the transversal axis.

Multiplicative Beamforming

It may be noticed with Fig-11(a,b) that the free field source maps seems to be disturbed compared to the smooth source distribution on Fig-10. Porteous et al. [3] invoked the

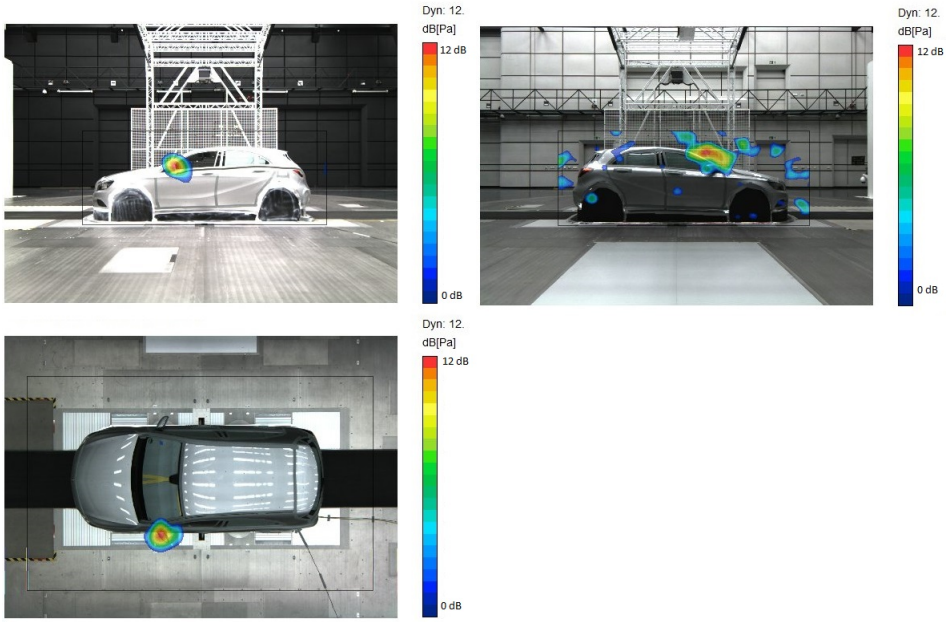

Fig. 10 - *2D CBF at 2 kHz with respectively left, right and top array.*

coherence loss between the three single arrays to explain this phenomenon and proposed a Multiplicative Beamforming (MBF) which consists in computing one independent CBF per array before merging the corresponding output maps in postprocessing. Considering N_a planar arrays, MBF can be seen as the geometric mean of each separate CBF map :

$$\mathbf{q}_{\text{mbf}} = \left(\prod_{l \leq N_a} \mathbf{q}_l \right)^{\frac{1}{N_a}} . \tag{18}$$

This approach was assessed on Fig-12. Considering the 12 dB level range used, it appears that the merging step of Eq.18 is not sharp enough to fade the sources erroneously introduced when using the single arrays separetely (see for example Fig-13).

Interestingly, the use of MBF with ESM FRF indicates with Fig-12(d) a spurious source on the opposit rear-view mirror. It should be stated here that the single array 3D imaging with realistic FRF is completely ill posed because of the masking effect brought by the transfer function. In the case under scrutiny in this section, the detection of a source on the left of the car with the right array only is almost impossible since the acoustic transfer is almost null because of the rigid car scattering behaviour. More theoretically, the column of $\mathbf{H}$ modelling the transfer between the prevailing source to localize and the array is almost zero and makes $\mathbf{H}$ poorly conditionned.

The intuitive solution is to use an array covering the object a completely as possible, which is almost the case when the three wind tunnel arrays are used together with the full CSM.

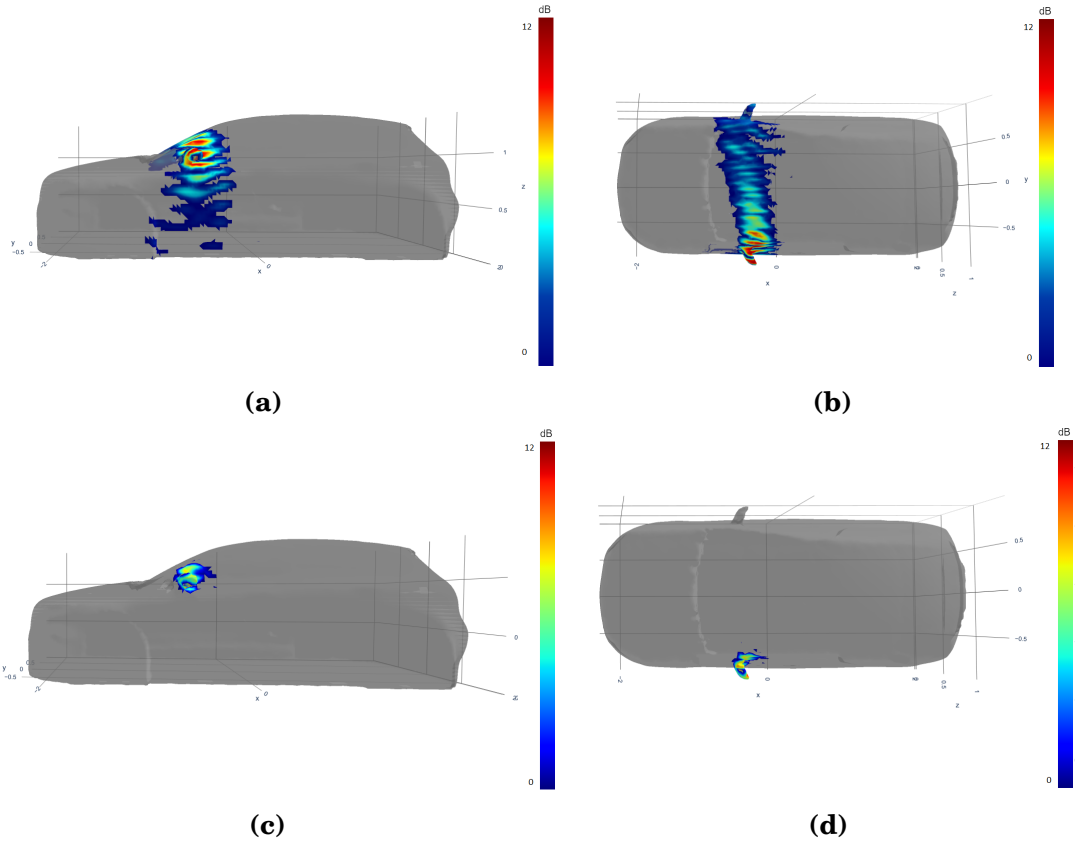

Fig. 11 - *3D CBF at 2 kHz using the full CSM, based on free field FRF (a,b) and ESM FRF (c,d)*

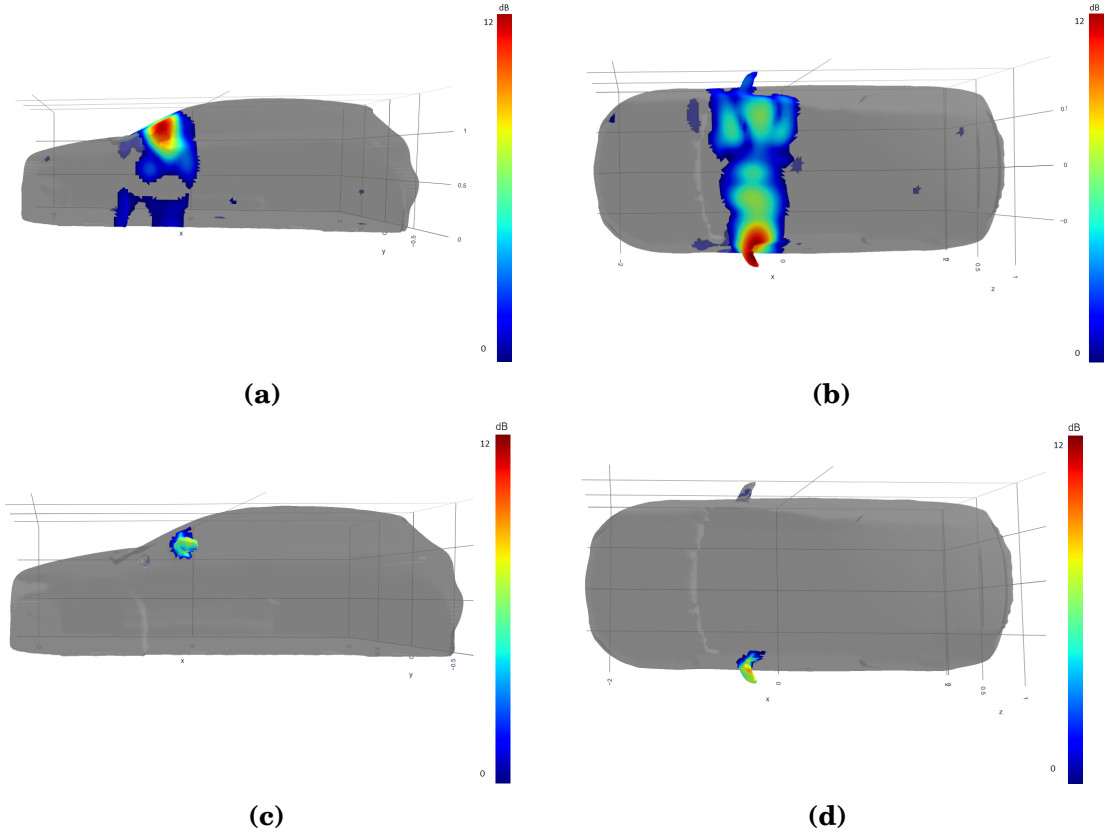

Fig. 12 - *3D MBF at 2 kHz using the 3 CSM separetely, based on free field FRF (a,b) and ESM FRF (c,d)*

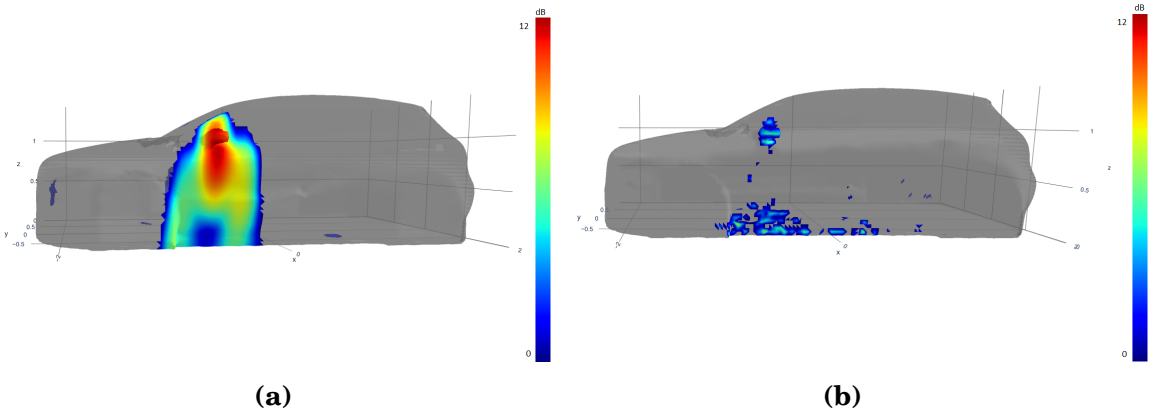

Fig. 13 - *3D CBF at 2 kHz using the top array only, based on free field FRF (a) and ESM FRF (b). The extended source area using the free field assumption illustrates the poor normal resolution of the planar array. The spurious sources that appears with the ESM based FRF are the result of the ill-posedness of the problem since the actual acoustic transfer between between the lower part of the car and the top array is almost zero.*

4.2 Beamforming including convection effects

At last, a similar study can be conducted to the same experimental set up with the wind tunnel activated at Mach 0.11 (140 km/h). A diagonal removal routine is applied to the CSM for denoising, and the ESM computation features the Amiet modification presented in section 3.2. The 2D CBF maps computed with *AAT* are given in Fig-14.

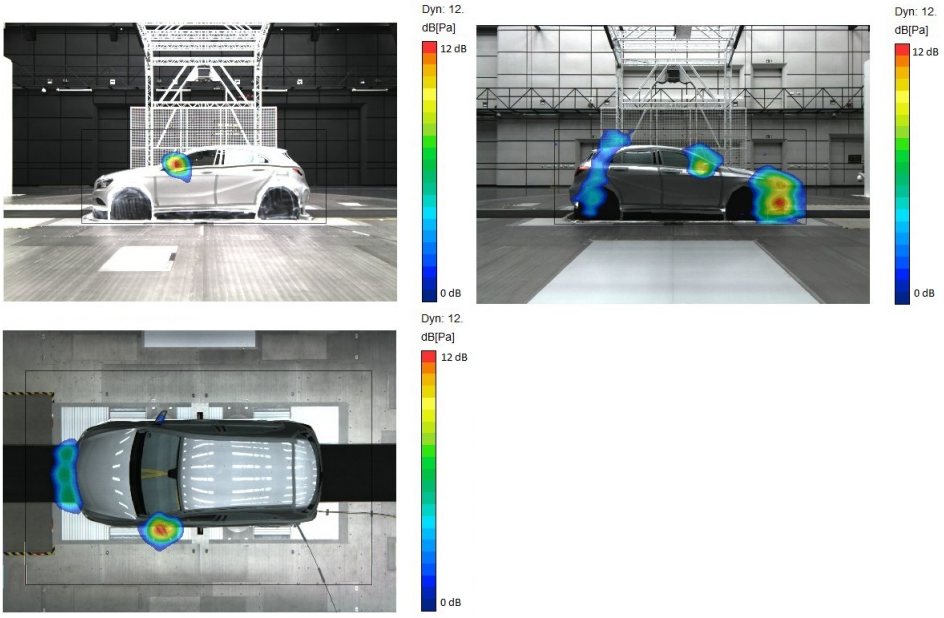

Fig. 14 - *2D CBF at 2 kHz with respectively left, right and top array at Mach 0.11*

Again, it can be observed on Fig-15 that the ESM approach achieves a strongest localization performance. The left array 2D CBF map on Fig-14 indicates that the aeroacoustic sources in front of the car are not supposed to be under the 12 dB dynamic range with respect to the artificial source direct level. Under the free field assumption, the unbaffled aspect of the source makes these aeroacoustic noise visible while results based on refined FRF remains clean.

Since the coherence loss between planar arrays is obviously higher with the presence of the shear layer, multiplicative beamforming assessed on Fig-16 provides significant improvements with free field beamforming. The ESM maps however are affected by the same issue as in the previous section : the right array induces error and damages the final result. It could be argued that the best option here would be to compute MBF with the left and top arrays only, but it would boil down to use a prior information on the source position seldom available during industrial studies.

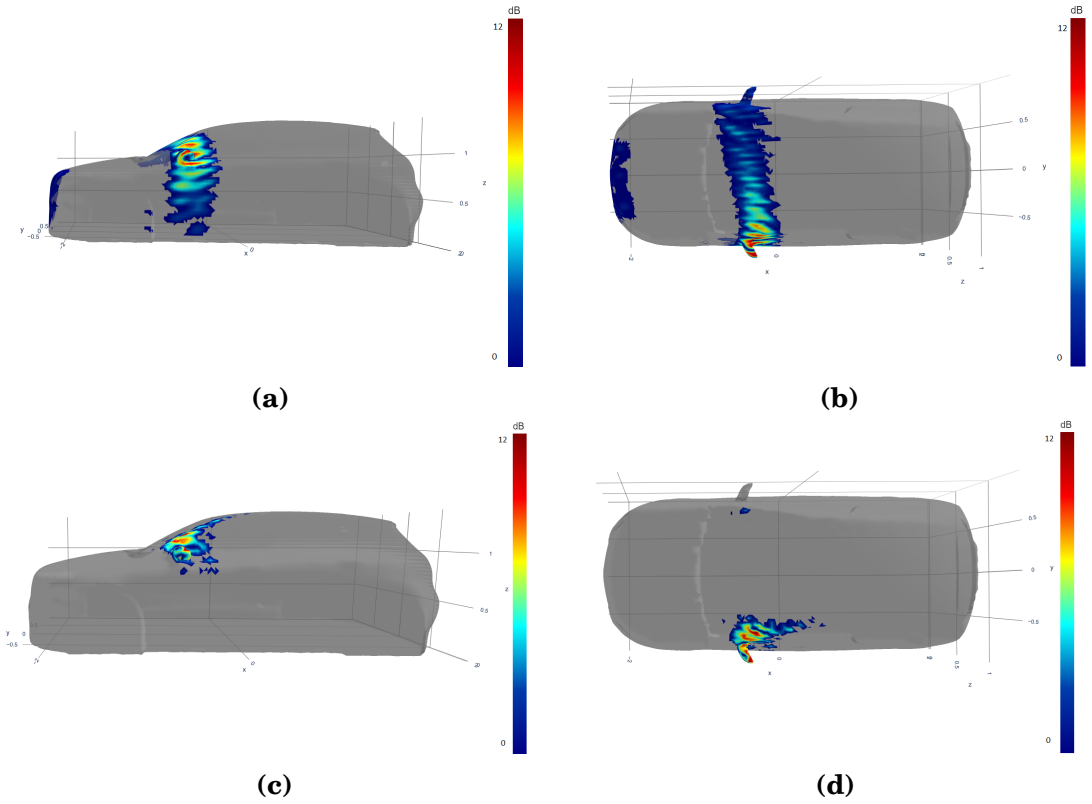

Fig. 15 - *3D CBF at 2 kHz using the full CSM, based on free field FRF (a,b) and ESM FRF (c,d)*

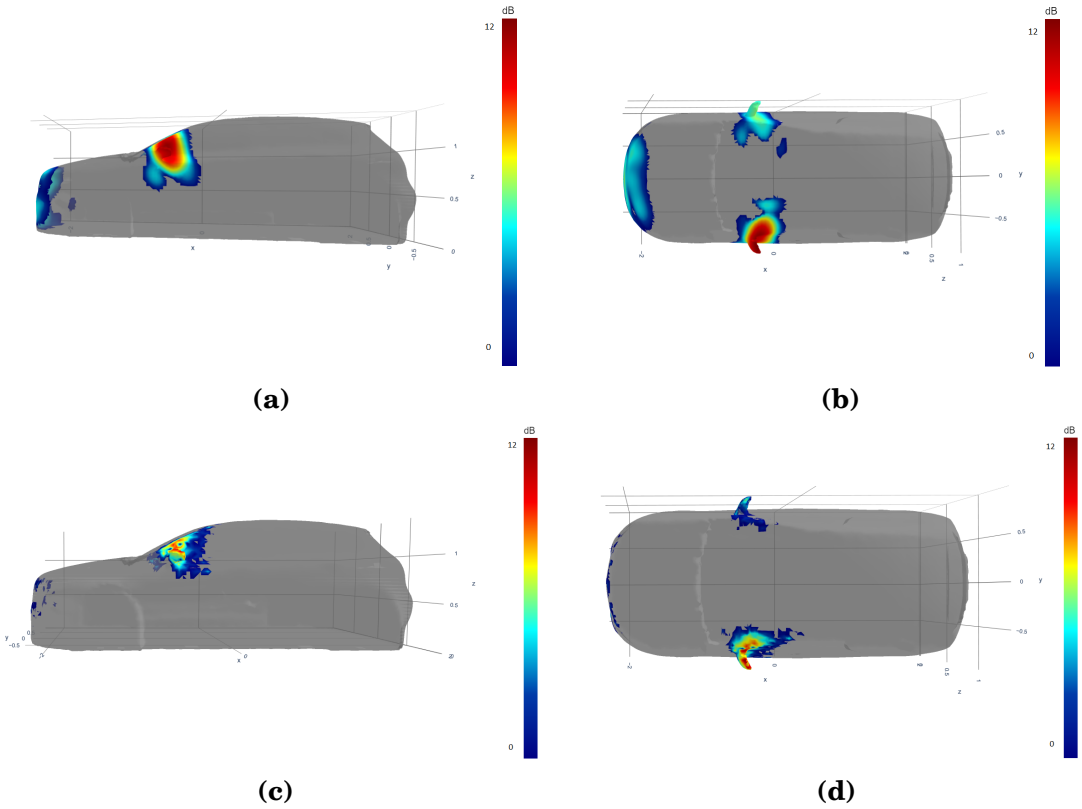

Fig. 16 - *3D MBF at 2 kHz using using the 3 CSM separetely, based on free field FRF (a,b) and ESM FRF (c,d) at Mach 0.11*

Conclusion

ESM provides a valuable model to improve 3D acoustic imaging results. Embedding an approximation of diffraction, reflections and shear layer refraction phenomena in the acoustic transfer function used to perform beamforming, it enhances the dynamic range and prevent misleading sources appearing when planar arrays poor normal resolution is used under a free field assumption.

Leads for further improvements are yet numerous. Quickly mentioned in this paper for the sake of brevity, the ESM in itself is an inverse problem and an in-depth parametric study of the equivalent sources type, amount and positions for the purpose of FRF computation would be worthwhile. Moreover, the question of coherence loss between remotes microphones when the three planar arrays are used at the same time remains. The arrays interspectra removal achieved with multiplicative beamforming tends indeed not to be very suitable with ESM transfer functions, and a model for coherence included in the ESM process would probably yields better results at this point.

Acknowledgements

Authors would like to thank Daimler AG for providing the measurements data recorded in the Daimler Wind Tunnel Centre in Sindelfingen.

References

[1] Gianmarco Battista. *Inverse methods for three-dimensional volumetric acoustic mapping*. PhD thesis, Universita Politecnica delle Marche, 2019.

[2] Thibaut Le Magueresse, Allan Outrequin, Mickaël Thivant, Jérôme Antoni, and Jean-Louis Jouvray. 3d acoustical characterization of an electrical engine by bayesian focusing. 8^{th} *Berlin Beamforming Conference*, 2020.

[3] Ric Porteous, Zebb Prime, Con. J. Doolan, Danielle J. Moreau, and Vincent Valeau. Three-dimensional beamforming of dipolar aeroacoustic sources. *Journal of Sound and Vibration*, 335:117–134, 2015.

[4] Gary H. Koopmann, Limin Song, and John B. Fahnline. A method for computing acoustic fields based on the principle of wave superposition. *Journal of the Acoustical Society of America*, 86:2433–2438, 1989.

[5] Gary H. Koopmann and John B. Fahnline. A numerical solution for the general radiation problem based on the combined methods of superposition and singular-value decomposition. *Journal of the Acoustical Society of America*, 90:2808–2819, 1991.

[6] Seongkyu Lee. Review: The use of equivalent source method in computational acoustics. *Journal of Computational Acoustics*, 25, 2017.

[7] Thibaut le Magueresse. *Approche unifiée multidimensionelle du problème d'identification acoustique inverse*. PhD thesis, LAUM & LVA, 2016.

[8] Thibaut Le Magueresse, Olivier Minck, Lucille Lamotte, Christophe Locqueteau, and Pascal Bouvet. Array based acoustic power measurement, renault pass-by noise. *Proceeding FISITA 2016*, 2016.

[9] Prasanga Samarasinghe and Thushara D. Abhayapala. Acoustic reciprocity: An extension to spherical harmonics domain. *Journal of the Acoustical Society of America*, 142:337–343, 2017.

[10] N.P. Valdivia and E.G. Williams. Study of the comparison of the methods of equivalent sources and boundary element methods for near field acoustic holography. *Journal of the Acoustical Society of America*, 120, 2006.

[11] P.A. Nelson and S.H. Yoon. Estimation of acoustic source strength by inverse methods : Part i, conditionning of the inverse problem. *Journal of Sound and Vibration*, 233:639–664, 2000.

[12] Benoît Oudompheng, Antonio Pereira, Christophe Picard, Quentin Leclère, and Barbara Nicolas. A theoretical and experimental comparison the iterative equivalent source method and the generalized inverse beamforming. 5^{th} *Berlin Beamforming Conference*, 2014.

[13] Antonio Pereira. *Acoustic imaging in enclosed spaces*. PhD thesis, INSA Lyon, 2013.

[14] Richard O. Duda and William L. Martens. Range dependence of the response of a spherical head model. *Journal of the Acoustical Society of America*, 104:3048–3058, 1998.

[15] Allan D. Pierce. *Acoustics - An introduction to its physical principles and applications*. McGraw-Hill, 1981.

[16] Mark H. Dunn and Ana F. Tinetti. Aeroacoustic scattering via the equivalent source method. *AIAA Aerospace Sciences Meeting*, 10, 2004.

[17] Nicolas Asquier. Calcul des fonctions de transfert acoustiques par la méthode des sources équivalentes. Technical report, UTC Compiègne, 2016.

[18] Mingsian R. Bai, Ching-Cheng Chen, and Jia-Hong Lin. On optimal retreat distance for the equivalent source method-based nearfield acoustical holography. *Journal of the Acoustical Society of America*, 129(3):1407–1416, 2011.

[19] Earl G. Williams. *Fourier Acoustics - Sound Radiation and Nearfield Acoustical Holography*. Academic Press, 1999.

[20] Nicolas P. Valdivia. Advanced equivalent source methodologies for near-field acoustic holography. *Journal of Sound and Vibration*, 438:66–82, 2018.

[21] Free Field Technologies. *Actran 2018 User's guide - Volume 1*, 2017.

[22] Jean-Christophe Autrique and Frédéric Magoulès. Studies of an infinite element method for acoustical radiation. *Applied Mathematical Modelling*, 30:641–655, 2006.

[23] R. K. Amiet. Refraction of sound by a shear layer. *Journal of Sound and Vibration*, 58:467–482, 1977.

[24] Thomas J. Mueller. *Aeroacoustic Measurements*. Springer, 2002.